earth

MDPI

Article

Comparison of GraphSAGE–Graph Attention Network and Best–Worst Method for Landslide Susceptibility Prediction Mapping

Aliasgar Hodaei [1], Saleh Salehi Fereidouni [2], Mostafa Khabazi [3], Mohammad Maleki [4], Poya Sohrabi [5,*], Amirbahador Damroodi [6] and Junye Wang [7]

[1] Department of Rescue and Relief, Iran Helal Applied Science Higher Education Institute, Tehran 15996-65111, Iran; dr.hodaei@helal-uast.ac.ir
[2] Key Laboratory of Urban Security and Disaster Engineering of Ministry of Education, Beijing University of Technology, Beijing 100124, China; salehsf86@yahoo.com
[3] Department of Geography, Tarbiat Modares University, Tehran 14117-13116, Iran; mostafakhabazi@modares.ac.ir
[4] Department of Remote Sensing & GIS, Kharazmi University, Tehran 15719-14911, Iran; std_mohammad.maleki@khu.ac.ir
[5] Department of Planning, Design, Technology of Architect, Sapienza University of Rome, 00196 Rome, Italy
[6] Department of Art and Architecture, Tarbiat Modares University, Tehran 14117-13116, Iran; d.amirbahador@modares.ac.ir
[7] Faculty of Science and Technology, Athabasca University, Athabasca, AB T9S 3A3, Canada; junyew@athabascau.ca
* Correspondence: poya.sohrabi@uniroma1.it

Abstract

Landslides, as a natural hazard, pose a potential risk to human life and infrastructure. However, predicting and mitigating landslide susceptibility is challenging due to the complexity of contributing factors, such as slope, groundwater level, earthquakes, and vegetation. This study aims to develop a GraphSAGE–Graph Attention Network (GraphSAGE-GAT) and Best–Worst Method (BWM) for predicting landslides and generating landslide susceptibility maps (LSMs) in Savadkouh County (northern Iran). For this purpose, twelve conditioning factors relevant to LSMs were considered: slope, faults, precipitation, vegetation, soil, watercourses, roads, cities, villages, elevation, and temperature. Receiver operating characteristic (ROC) curves were used to evaluate model performance based on the number of events in the landslide susceptibility classes, as well as the Precision–Threshold curve, Recall, Precision, and Specificity across all possible thresholds. The most important factor in the BWM was slope, with 22.63%. By combining weights and layers in GIS, LSMs were generated using both BWM and GraphSAGE-GAT. The results show that 47% of the landslide points were classified as high susceptibility (high and very high) by BWM, whereas 67.33% were classified as high susceptibility by GraphSAGE-GAT. Furthermore, BWM achieved a maximum Precision of approximately 73%, while the Precision of GraphSAGE-GAT increased with the threshold and approached 100% at very high threshold values. The area under the ROC curve was 0.544 for BWM and 0.836 for GraphSAGE-GAT, demonstrating the substantially better discriminatory performance of GraphSAGE-GAT. Therefore, GraphSAGE-GAT integrated with GIS provides an effective approach for assessing landslide susceptibility, and the results are promising because the model not only provides good discrimination between susceptible and non-susceptible areas but also generates LSMs that capture spatial relationships among landslide-conditioning factors at the county scale.

Academic Editor: Christian Conoscenti

Received: 6 September 2026
Revised: 25 October 2026
Accepted: 28 October 2026
Published: 1 November 2026

Copyright: © 2026 by the author. Licensee MDPI, Basel, Switzerland. This article is an open access article distributed under the terms and conditions of the Creative Commons Attribution (CC BY) license.

Keywords: natural hazard; deep learning; GraphSAGE–graph attention network; best–worst method; landslide susceptibility prediction

1. Introduction

Landslides cause serious damage every day and directly threaten human lives [1]. Landslides result in billions of dollars in damage and fatalities, including economic losses and numerous casualties annually [2,3]. Landslides are becoming more frequent and destructive due to extreme weather events, natural disasters, and the impacts of anthropogenic disturbance in landslide-prone areas [4]. Therefore, investigating and predicting potentially high-sensitivity areas are of critical value to mitigate and reduce the damage and harm caused by landslides [5–8]. Landslides are triggered by changes in earth processes, such as heavy rainfall, flooding, groundwater levels, surface water saturation, earthquakes, slope, lithology, soil type, human activities, and vegetation [9–12]. Given the variability of these processes, it is necessary to predict potential landslide areas over space and time [13]. Predicting where and when landslides are likely to occur in specific locations and regions of interest remains a key challenge in natural hazards research and mitigation because these complex factors are not always identifiable [14–17].

Landslide susceptibility maps (LSMs) using multiple spatial layers are key for the development of early warning systems to prevent catastrophic landslides, as the spatial conditions and processes are associated with environmental hazards [18–21]. Geographic Information Systems (GISs) can collect, process, and combine spatial layers, as well as map potential sensitive areas for managers' decision-making [22–24]. This provides a tool for further processing in the field of multi-criteria decision-making (MCDM) and deep learning (DL) [25,26]. Due to the multi-criteria nature of potential landslide-sensitive factors, MCDM and DL combined with GISs are advanced approaches for predicting landslide sensitivity and generating LSMs [27,28]. MCDM models, such as the Analytic Hierarchy Process (AHP) and the Best–Worst Method (BWM), can integrate the decision-making process and expert opinions to determine the relative importance of criteria as decision-making inputs while combining GIS capabilities [29–31]. In recent years, the rapid growth of spatial big data and advances in computational resources have promoted the widespread application of DL techniques in geospatial analysis and sensitivity mapping [32,33]. Unlike conventional machine learning (ML) algorithms, deep learning models are capable of automatically learning hierarchical feature representations from complex and high-dimensional datasets, enabling them to capture intricate nonlinear relationships and spatial dependencies [34]. Consequently, various DL architectures, including Convolutional Neural Networks (CNNs), Recurrent Neural Networks (RNNs), Graph Neural Networks (GNNs), and Transformer-based models, have been successfully employed for landslide susceptibility mapping and other environmental modeling tasks [35–39].

In recent years, multi-criteria decision-making (MCDM) and deep learning techniques have been increasingly applied to landslide susceptibility mapping and detection. Gigović et al. (2019) integrated GIS and the Best–Worst Method (BWM), demonstrating the applicability of expert-based criteria weighting for susceptibility mapping in Serbia [40]. Moharrami et al. (2020) applied fuzzy BWM in Austria, achieving AUC values of 0.93 for success rate and 0.89 for prediction rate, outperforming fuzzy AHP [41]. Ghorbanzadeh et al. (2019) evaluated machine learning algorithms and CNNs for landslide detection in Nepal using an independent test zone [42]. Similarly, Prakash et al. (2020) developed a modified U-Net with ResNet34 blocks in Oregon, which outperformed conventional pixel- and object-based methods, achieving a Matthews correlation coefficient of 0.495 and a probability of detection of 0.72 [43]. Together, these studies demonstrate the potential of

both MCDM and deep learning for landslide assessment, while highlighting differences in their methodological approaches and predictive capabilities.

Despite the successes of both MCDM and DL techniques, issues remain to be resolved. For example, DL depends on the quantity and quality of training data, potential overfitting, and the choice of prediction models for predicting landslide-prone areas, while MCDM depends on expert opinions. Given the importance of landslides, further research should address: (1) comparison of DL and MCDM models for better model selection; (2) predictions of occurrence and runout of large slope failures; and (3) generation of LSMs at the regional scale.

The aim of this study is to investigate the capability of MCDM and DL to predict landslide susceptibility in landslide-prone areas. The BWM was used as a representative of MCDM, and the GraphSAGE Graph Attention Network (GraphSAGE-GAT) algorithm was used as a representative of DL. The spatial layers of criteria and the data of actual landslide points were input into the models to predict susceptibilities. This study should guide the wider application of advanced approaches in regional landslide prediction and LSM generation.

2. Materials and Method

2.1. Study Area

Savadkouh County is located in Mazandaran Province (northern Iran), bordering Qaemshahr to the north, Babol to the west, Dodangeh Sari to the east, and the Alborz Mountain Range (Tehran and Semnan Provinces) to the south (Figure 1). The county is situated between latitudes 35°49′ and 36°23′ N and longitudes 52°39′ and 53°14′ E [44]. According to the latest census (2016), the county has a population of 43,913 and an area of 2078 square kilometers [45]. The county consists of 4 rural districts and 40 villages, which constitute 57% of the county's population, and is one of the most important counties in Mazandaran Province due to its location on the route from Tehran to the north, the national railway, and the presence of industrial units [46]. The altitude of the county ranges from 103 to 3746 m above sea level. Figure 1 presents the study area and its location in Iran. Figure 1a shows the position of Mazandaran Province in northern Iran, Figure 1b illustrates the location of Savadkuh County within Mazandaran Province, and Figure 1c shows a satellite image of Savadkuh County along with the distribution of recorded landslide occurrences.

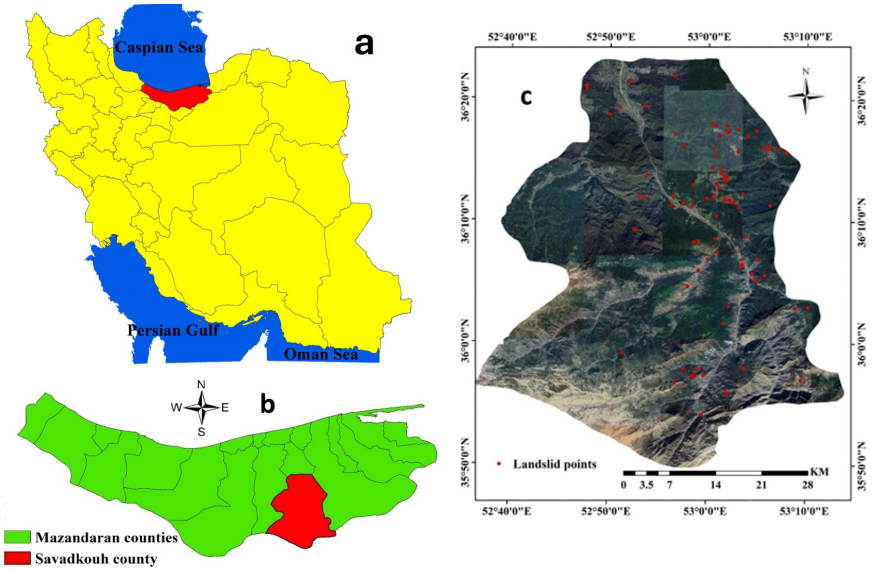


Figure 1. Study area and location: (**a**) Iran, (**b**) Mazandaran Province, and (**c**) Savadkouh County.

2.2. Landslide Criteria

Twelve criteria were used in this study, including the slope of the lithological unit, faults, precipitation, vegetation, soil, watercourses, roads, cities, villages, elevation, and temperature. A digital elevation model (DEM) was used to prepare the slope and elevation layers. Lithological maps and soil and vegetation types were obtained from the relevant organizations, while village and road data were derived in GIS. Precipitation and temperature data were also obtained from the Meteorological and Hydrological Organization and were interpolated using the Kriging method. Data were obtained from the relevant organizations in 2025 (in accordance with Table 1). Table 1 presents the criteria used, role in landslide susceptibility assessment, data source, processing method, and resolution.

Table 1. Landslide-conditioning factors, data sources, and processing methods used in this study.

Code	Criterion	Role in Landslide Susceptibility Assessment	References	Data Source and Processing Method	Resolution
C1	Slope	Steeper slopes increase gravitational stress, making slope materials more prone to failure.	[47]	Army Geographical Organization; DEM processing to derive slope layer.	30 × 30 m
C2	Lithology	Different lithological units exhibit varying mechanical strength and weathering characteristics, which strongly influence slope stability.	[48]	Geological Survey; lithological data converted from polygon to raster format.	30 × 30 m
C3	Distance from Fault	Areas located closer to faults are generally more fractured and unstable and may also be affected by higher seismic activity, increasing landslide likelihood.	[49]	Geological Survey; Euclidean distance analysis applied to fault layer.	30 × 30 m
C4	Rainfall	High or intense rainfall raises pore-water pressure and reduces soil shear strength, acting as a primary trigger for landslides.	[50]	Meteorological Organization; precipitation isohyet data interpolated using the Kriging method.	30 × 30 m
C5	Vegetation	Dense vegetation enhances slope stability through root reinforcement, whereas sparse vegetation increases vulnerability to erosion and mass movement.	[51]	Forests, Rangelands and Watershed Management Organization; vegetation data converted from polygon to raster format.	30 × 30 m
C6	Soil Types	Soil texture, structure, and cohesion control permeability and shear strength, influencing slope response to loading and rainfall infiltration.	[52]	Soil and Water Research Institute; soil type data converted from polygon to raster format.	30 × 30 m
C7	Distance from Watershed	Proximity to rivers and streams promotes toe erosion, undercutting, and material saturation, which weaken slope stability.	[53]	Derived from DEM; Euclidean distance analysis applied to river network.	30 × 30 m
C8	Distance from Road	Road construction modifies slope geometry, drainage patterns, and loading conditions, often creating artificial instability.	[54]	Surveying Organization; Euclidean distance analysis applied to road network.	30 × 30 m

C9	Distance from City	Urban development increases surface load and alters natural drainage systems, thereby raising landslide susceptibility in adjacent slopes.	[55]	Statistical Center of Iran; Euclidean distance analysis applied to urban areas.	30 × 30 m
C10	Distance from Village	Village areas, though smaller in scale than cities, involve human activities such as construction and agriculture that disturb natural slope equilibrium.	[56]	Statistical Center of Iran; Euclidean distance analysis applied to villages.	30 × 30 m
C11	Elevation	Higher elevations are often associated with steeper terrain, freeze–thaw cycles, and distinct climatic conditions that affect slope stability.	[57]	Army Geographical Organization; DEM used to derive elevation layer.	30 × 30 m
C12	Temperature	Temperature variations influence weathering intensity, freeze–thaw processes, and soil moisture conditions, all of which contribute to landslide susceptibility.	[58]	Meteorological Organization; temperature isotherm data interpolated using the Kriging method.	30 × 30 m

2.3. Best–Worst Method (BWM)

The BWM is a multi-criteria decision-making (MCDM) method in which multiple alternatives are evaluated according to multiple criteria to: (a) select the best alternative among a set of alternatives, (b) rank all the alternatives, or (c) classify the alternatives into several categories. BWM is a pairwise comparison-based method that provides a structured way to determine the weights of criteria, from the best criterion to all others and from all others to the worst criterion. Specifically, it can be used to evaluate alternatives according to the criteria to determine the importance (weight) of each criterion, which is then used to find a solution that satisfies the main goal(s) of the problem. Thus, the weights of each criterion are calculated with a high degree of consistency.

Given the inherent diversity of the criteria used, multiple experts with related backgrounds (the experts' information is presented in Table 2) were invited to provide their judgments on the criteria in order to perform the comparison using the BWM. The criteria were reviewed by experts and, through a survey process, one criterion was selected as the best and one as the worst. Subsequently, each expert compared the remaining criteria with the best and worst criteria. To achieve consensus among the experts and aggregate all individual matrices into the final matrix, the average of the matrices were employed.

Table 2. Experts' information.

Experts' Backgrounds	Geology	RS & GIS	Environmental Hazards	Geomorphology	Soil Sciences	Hydrology
Number	3	2	2	2	1	1

The BWM can be implemented as follows [59,60]:

Phase 1: Identify a decision criterion set (C_1, C_2, C_3, … C_n).

Phase 2: Select the best criterion B and the worst criterion W.

Phase 3: Compare the best criterion to all other criteria, indicating the best priority. Then, a best-to-other vector is obtained as follows:

$$A_B = (A_{B1}, A_{B2}, \ldots A_{Bn}) \quad (1)$$

where A_{BJ} is the priority of B over criterion j and $A_{BB} = 1$

Phase 4: Compare all other criteria to the worst criterion, indicating the priority of all the criteria over W. Then, an other-to-worst vector is determined as follows:

$$A_B = (A_{1w}, A_{2w}, \ldots A_{nw})^T \quad (2)$$

where A_{JW} denotes the priority of criterion j over W and $A_{ww} = 1$.

Phase 5: Utilize the comparison results to calculate the weights for each criterion (i.e., $W_1^*;\ W_2^*;\ W_n^*$). For the pairs of W_B/W_J and W_J/W_W, the goal is to minimize the inconsistency in the judgments to identify the optimal weights. An optimal weight is a value that yields $W_B/W_J = A_{BJ}$ and $W_J/W_W = A_{JW}$. Thus, for every j value, it minimizes the maximum absolute differences of $\left|\frac{W_B}{W_J} - A_{BJ}\right|$, and $\left|\frac{W_J}{W_W} - A_{JW}\right|$ for all j is minimized. Because the weights are non-negative and summed, a unique solution can be obtained as

$$Min \max_j \left\{\left|\frac{W_B}{W_J} - A_{BJ}\right|, \left|\frac{W_J}{W_W} - A_{JW}\right|\right\} \quad (3)$$

when $\sum_j W_j = 1$,

$W_j \geq 0$ for all j.

Equation (1) is identical to the following:

$$\min \xi$$

$$\left|\frac{W_B}{W_J} - A_{BJ}\right| \leq \xi \text{ for all } j \quad (4)$$

$$\left|\frac{W_J}{W_W} - A_{JW}\right| \leq \xi \text{ for all } j \quad (5)$$

$$W_j \geq 0 \text{ for all } j$$

The optimum values ($W_1^*;\ W_2^*;\ W_n^*$) and the consistency index ξ^* are calculated using the above equations. The maximum values of the consistency index, ξ, correspond to A_{BW}, as shown in Table 3. The consistency rate varies with the priority from the best to the worst index and can be calculated using Equation (6) [61,62].

$$Consistency\ rate = \frac{\xi^*}{consistency\ index} \quad (6)$$

Table 3. Values for calculation of the consistency index.

A_{BW}	**1**	**2**	**3**	**4**	**5**	**6**	**7**	**8**	**9**
Consistency index (ξ)	0.00	0.44	1.00	1.63	2.30	3.00	3.73	4.43	5.23

The consistency index quantifies the logical consistency in pairwise comparisons.

2.4. GraphSAGE–Graph Attention Network (GraphSAGE-GAT)

In recent years, Graph Neural Networks (GNNs) have emerged as one of the most advanced deep learning approaches for analyzing graph-structured data [63,64]. Unlike conventional machine learning algorithms, which process each sample independently, GNNs incorporate both the intrinsic characteristics of each sample and the relationships among neighboring samples during the learning process. One of the most influential developments in this field is GraphSAGE, proposed by Hamilton et al. (2017), which enables inductive learning by aggregating information from neighboring nodes and allows the trained model to generalize to unseen data [65]. Subsequently, Veličković et al. (2017) introduced the Graph Attention Network (GAT), which incorporates an attention mechanism to adaptively assign different importance weights to neighboring nodes during feature aggregation [66]. Considering the complex spatial characteristics of landslide

occurrence, a hybrid GraphSAGE-GAT architecture was adopted in this study to simultaneously model environmental features and the relationships among neighboring pixels.

During the data preparation stage, all raster layers representing landslide-conditioning factors were converted into a feature matrix, where each valid pixel was treated as a graph node. Pixels containing missing values were excluded from the analysis. Continuous variables, including elevation, slope, rainfall, distance to faults, distance to roads, distance to rivers, temperature, distance to villages, and distance to cities, were directly incorporated into the model. Categorical variables, including lithology, soil type, and land-cover type, were transformed into binary variables using one-hot encoding. Standardization parameters were estimated from the training set and subsequently applied to the test set to prevent data leakage and ensure an unbiased evaluation. To eliminate differences in variable scales, all continuous variables were standardized using Z-score normalization:

Equation (7) transforms all continuous variables to a common scale with zero mean and unit variance, thereby preventing variables with larger numerical ranges from dominating the optimization process.

$$z_i = \frac{x_i - \mu}{\sigma} \tag{7}$$

Here, z_i is the standardized value of the ith observation, x_i is the original value of the feature, μ denotes the mean of the corresponding feature, and σ represents its standard deviation.

After feature normalization, a graph was constructed using the K-nearest neighbors (KNN) algorithm, where each node was connected to its 10 nearest neighbors. This neighborhood size was selected to preserve local spatial connectivity while avoiding excessive graph density. A smaller value of (k) could produce a sparsely connected graph with insufficient neighborhood information, whereas a substantially larger value could increase graph density and introduce less relevant connections, potentially diluting local patterns. The GraphSAGE layer generated node embeddings by aggregating information from neighboring nodes according to the equation below.

Equation (8) updates each node representation by combining its own features with the averaged information of neighboring nodes, enabling the model to capture local spatial dependencies and contextual relationships.

$$h_i^{l+1} = \sigma\left(W^{(l)} \cdot Mean\left(\left\{h_i^{(l)}\right\} \cup \left\{h_i^{(l)} \mid j \in N(i)\right\}\right)\right) \tag{8}$$

Here, $h_i^{(l)}$ denotes the feature representation of node (i) at layer (l), ($N(i)$) is the set of neighboring nodes connected to node (i), $W^{(l)}$ is the learnable weight matrix, Mean() denotes the neighborhood aggregation function, and $\sigma(.)$ is the nonlinear activation function.

The node embeddings were subsequently fed into the Graph Attention Network (GAT), where the contribution of each neighboring node was adaptively determined through an attention mechanism:

Equation (9) enables the network to assign larger weights to more informative neighboring nodes while reducing the influence of less relevant neighbors, thereby improving feature aggregation in heterogeneous spatial environments.

$$a_{ij} = \frac{\exp\left(LeakyReLU\, a^T[Wh \| Wh_i]\right)}{\sum_{k \in N(i)} exp\left(LeakyReLU\, a^T[Wh \| Wh_k]\right)} \tag{9}$$

Here, a_{ij} is the normalized attention coefficient assigned to neighboring node (j), a is the learnable attention vector, W denotes the shared linear transformation matrix, h_i and h_j are the feature vectors of nodes (i) and (j), respectively, and $\|$ represents vector concatenation.

The final network architecture consisted of a GraphSAGE layer with 64 hidden neurons, followed by a two-head GAT layer with 32 hidden units per attention head, and a Softmax output layer that converted network outputs into class probabilities for binary classification. The model was trained for 300 epochs using the Adam optimizer, with a learning rate of 0.001 and a weight decay of 5×10^{-4}, providing stable convergence during optimization. To mitigate the effect of class imbalance, the weighted cross-entropy loss function was employed.

Equation (10) assigns larger penalties to misclassified samples from the minority class, thereby improving the model's ability to identify landslide pixels despite the highly imbalanced distribution of landslide and non-landslide samples.

$$L = -\sum_{c=1}^{2} w_c y_c \log(p_c) \quad (10)$$

Here, (L) is the weighted cross-entropy loss, w_C is the weight assigned to class (c), y_c is the ground-truth label, and p_c is the predicted probability of class (c).

After training, the optimized model was applied to all valid pixels within the study area. To improve computational efficiency and reduce memory consumption, the prediction process was performed in batches of 50,000 pixels. Finally, the predicted probabilities of landslide occurrence were converted into a continuous landslide susceptibility map.

Training and Testing

The landslide inventory comprised 101 recorded events obtained from ground-based monitoring by the Geological Survey of Iran, with locations surveyed using multi-frequency GPS receivers and represented as point features corresponding to the geometric centers of the landslide occurrences. The dataset was constructed using the 101 mapped landslide points as positive samples and randomly selected non-landslide pixels as negative samples. To address class imbalance, the number of negative samples was set to a maximum of 20 times the number of positive samples, using a fixed random seed (42) to ensure reproducibility. The resulting dataset was divided into training (80%) and testing (20%) subsets using stratified random sampling, preserving the class proportions in both subsets. The training subset was used to construct the graph and train the GraphSAGE–GAT model, while the testing subset was reserved for independent model evaluation. Feature standardization was applied before model training. Landslide points were converted into positive raster samples by assigning each point to its corresponding raster cell, while valid cells without mapped landslides were treated as candidate negative samples. Negative samples were drawn randomly from valid raster cells across the study area, without spatial stratification or minimum-distance constraints. The random split did not enforce spatial separation; therefore, potential spatial dependence between training and testing samples remains a limitation.

2.5. Model Validation

A set of quantitative indicators and performance graphs was used to validate the *GraphSAGE-GAT* and BWM models in susceptibility prediction. The most important evaluation tool was the receiver operating characteristic (ROC) curve, which is plotted based on the relationship between Recall and Specificity at different thresholds [67]. The area under the ROC curve (*AUC*) was used as an overall indicator of the model's discriminative ability. A value closer to 1 indicates higher model accuracy [68]. To examine the model's accuracy at different threshold levels, a Precision–Threshold graph was used, which displays the model's ability to distinguish between events and non-events at various thresholds [69]. In addition, the classical measures of Precision, Recall, and Specificity were calculated quantitatively [70,71]. These measures were derived from the Confusion Matrix. The following Equations (11)–(15) present the validation relationships:

$$Precision = \frac{TP}{TP + FP} \quad (11)$$

$$Recall = \frac{TP}{TP + FN} \quad (12)$$

$$Specificity = \frac{TN}{TN + FP} \quad (11)$$

where *TP* is the number of true positives, *TN* is the number of true negatives, *FP* is the number of false positives, and *FN* is the number of false negatives.

The ROC curve represents the diagnostic ability of a classifier, plotted by varying the decision threshold and calculating the true-positive rate (*TPR*) versus the false-positive rate (FPR) [72,73]. The *AUC* provides a scalar value that quantifies the probability that a randomly selected positive sample will be ranked higher than a randomly selected negative sample [74]. *AUC* values range from 0.5 (no discriminative power) to 1.0 (perfect discrimination).

$$AUC = \int_0^1 TPR(FPR)dFPR \quad (12)$$

Here, *TPR* is *Recall* and *FPR* = 1 − *Specificity* as in Equation (15).

$$FPR = \frac{FP}{FP + TN} = 1 - Specificity \quad (13)$$

3. Results and Discussion

The landslide susceptibility values produced by the BWM and GraphSAGE-GAT models were reclassified into five classes: very low, low, moderate, high, and very high. Classification was performed using the natural breaks (Jenks) method, which groups continuous susceptibility values into statistically optimal intervals. This approach is widely used in landslide studies to create susceptibility classes.

3.1. Landslide Criteria and Weights

Figure 2 presents the maps of the criteria used in Savadkuh County. Figure 2a shows the soil types, with Alfisols covering the largest area, followed by Mollisols and rock outcrops, while Inceptisols occupy a small area in the south. Figure 2b illustrates the distance from rivers, indicating four main rivers with numerous tributaries flowing from south to north; most areas are within 2000 m of a river, while distances in the southern part reach up to 4000–5500 m. Figure 2c shows the altitude, which decreases from south to north, ranging from 3746 m above sea level in the southwest to 103 m in the northwest. Figure 2d presents the annual temperature map, with temperatures between 1 and 14 °C, increasing from south to north, and the largest area falling within 10–14 °C. Figure 2e depicts the road network, with main roads running south to north toward Sari, connected by secondary roads, and the greatest distances occurring in the mountainous southwest. Finally, Figure 2f shows precipitation, ranging from 500 to 1200 mm, with lower rainfall in the high-altitude south and higher rainfall in the northern lowlands due to proximity to the sea and higher humidity.

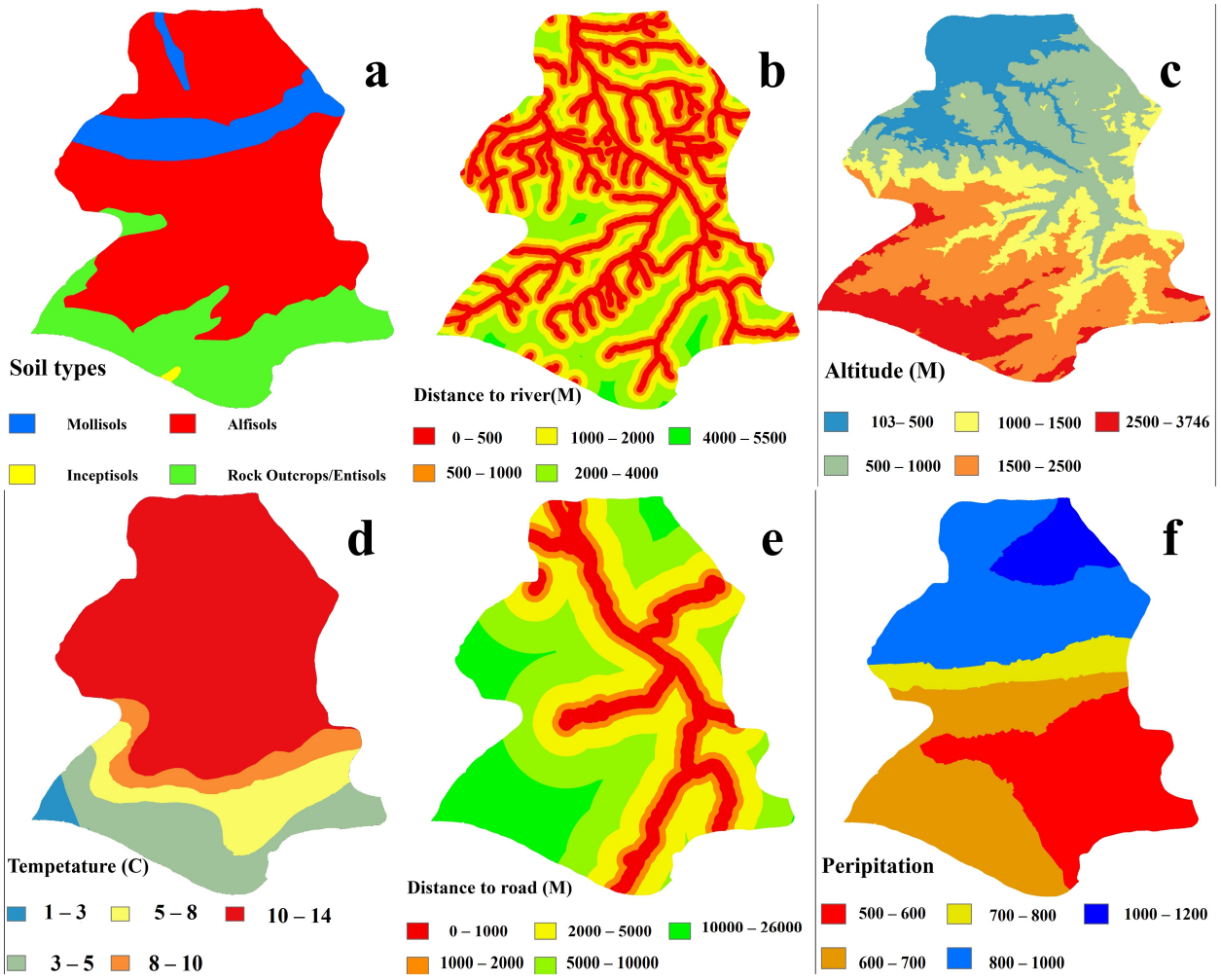


Figure 2. Criteria maps: (**a**) soil types, (**b**) distance to rivers, (**c**) altitude, (**d**) temperature, (**e**) distance to road, and (**f**) precipitation.

Figure 3 presents additional criteria maps for Savadkuh County. Figure 3a shows that forest covers most of the northern area. Figure 3b illustrates the slope, which is higher in the south and gradually decreases toward the north, with most areas exceeding 20% slope and only small portions ranging from 0 to 2%. Figure 3c shows the fault distribution, indicating that a large part of the area is within 500 m of a fault, while faults are sparse in the southern region. Figure 3d depicts 25 lithological units, with three units covering the majority of the area: TRJS (about half of the area), followed by MM and KZIZ. The city of Savadkuh is located along a valley beside the river, and Figure 3e illustrates the Euclidean distance from the city in a radial pattern. Figure 3f shows the distance from villages, indicating that villages are distributed across most of the county except for some northern and southern parts; village density is highest in the north and northwest, and the distribution is more uniform in the eastern half than in the western half.

Tables 4 and 5 present the BWM pairwise comparison matrices for the criteria used in this study. According to these matrices, the most important criterion is slope, while the least important criterion is temperature. Table 4 displays the importance of slope (the best criterion) relative to the other criteria, with C12 representing the worst criterion among the remaining ones. Table 5 shows the importance of all other criteria relative to C12 (the worst criterion), where C1 is identified as the most significant compared to the rest.

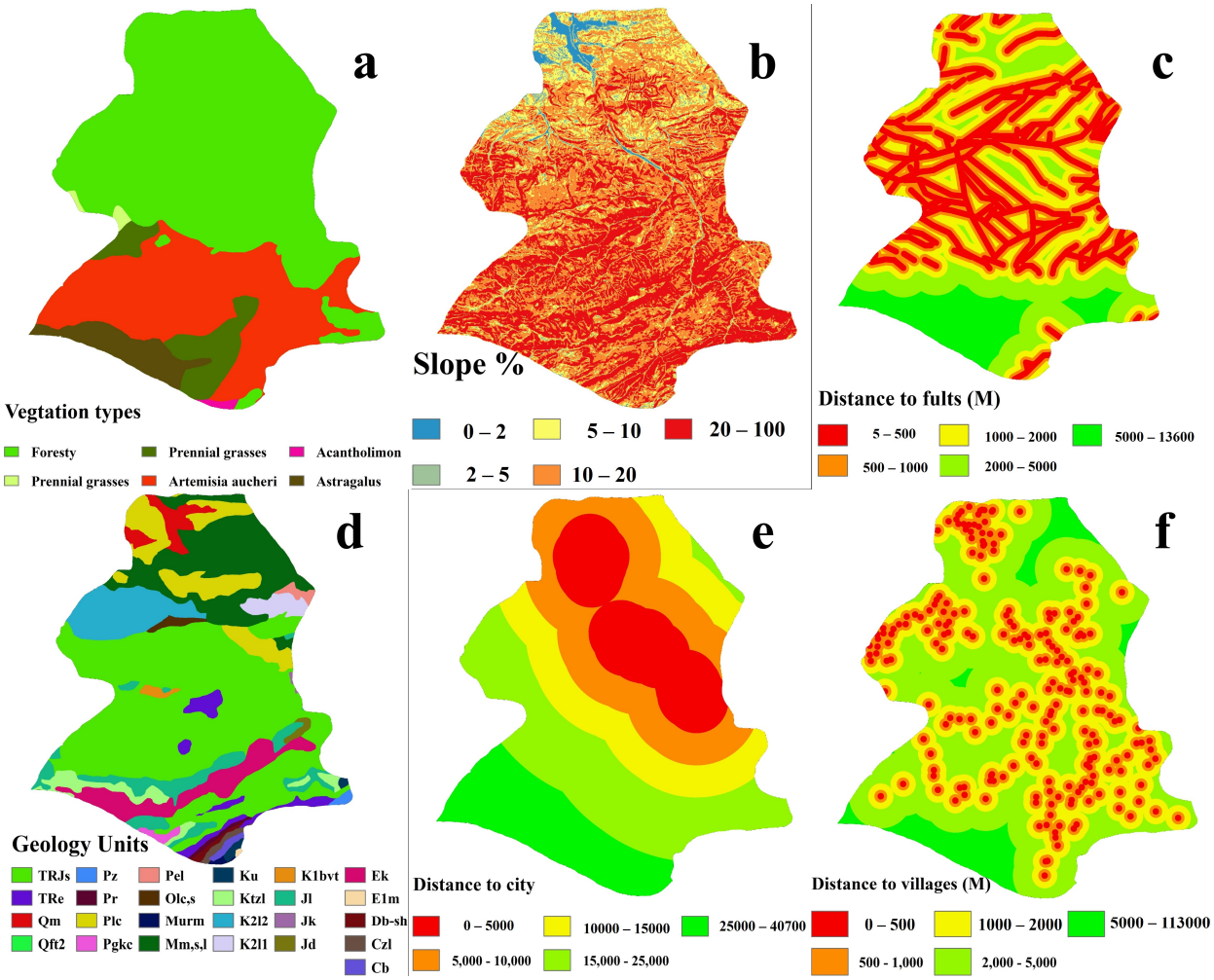


Figure 3. Criteria maps: (**a**) vegetation types, (**b**) slope, (**c**) distance to fault, (**d**) geology unit, (**e**) distance to city, and (**f**) distance to village.

Table 4. The superiority of the best criterion (C1) over other criteria.

Criteria	C2	C3	C4	C5	C6	C7	C8	C9	C10	C11	C12
Weight	2	2	3	3	4	5	6	6	7	8	9

Table 5. The superiority of other criteria over the worst criterion (C12).

Criteria	C1	C2	C3	C4	C5	C6	C7	C8	C9	C10	C11
Weight	9	8	7	7	6	5	5	4	3	2	2

Figure 4 presents the weight chart of the twelve criteria derived from the BWM weighting process. After obtaining the optimal pairwise comparisons and solving the BWM optimization model, the normalized weights of the conditioning factors were extracted and plotted to visually illustrate their relative influence on landslide susceptibility. The results show that slope, lithology, and distance from the fault are the three most important criteria for predicting landslide occurrence, with weights of 22.63, 13.7, and 13.7, respectively. In contrast, temperature, altitude, and distance from villages are the least important criteria, with weights of 1.99, 3.42, and 3.91, respectively. The inconsistency index was 0.0447, indicating a high degree of consistency in the model.

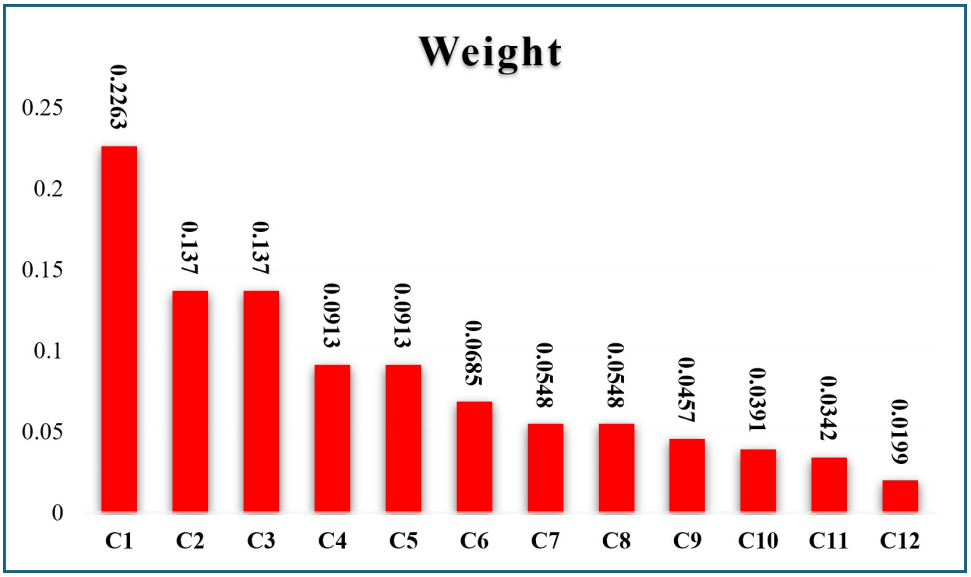


Figure 4. Weights of the twelve criteria.

3.2. Landslide Susceptibility Mapping (LSM)

Figure 5a shows the landslide susceptibility map of Savadkouh County generated using the BWM, classified into five susceptibility classes ranging from very low to very high. The spatial distribution of susceptibility is heterogeneous across the county. The southwestern part of the study area is predominantly characterized by very low susceptibility, whereas a broad zone of high to very high susceptibility extends from west to east in the central and southern parts of the county. The relatively high susceptibility in these areas can be attributed primarily to the presence of steep slopes and unfavorable terrain conditions. In contrast, large portions of the county are classified as having medium susceptibility, indicating areas where a combination of environmental factors creates moderate landslide potential. Overall, the BWM results indicate that susceptibility is strongly controlled by the spatial distribution of the conditioning factors and their assigned weights. Figure 5b presents the landslide susceptibility map generated using the GraphSAGE–GAT model. In contrast to the relatively continuous pattern observed in the BWM map, the GraphSAGE–GAT model produces a more spatially differentiated susceptibility pattern, with very low susceptibility covering a large proportion of the county, particularly across the southwestern, western, and central–southern regions. Areas of high and very high susceptibility are mainly concentrated in the northern and northeastern parts of the county, with additional localized high-susceptibility zones distributed across the central and eastern regions. The concentration of observed landslide points within these high- and very-high-susceptibility zones indicates a strong spatial correspondence between the model predictions and the actual landslide inventory. The ability of GraphSAGE–GAT to incorporate both environmental attributes and spatial relationships among neighboring pixels may explain its more localized identification of high-sensitivity areas. Compared with BWM, the GraphSAGE–GAT map therefore provides a more spatially heterogeneous representation of landslide susceptibility, particularly in areas where landslide occurrences are concentrated.

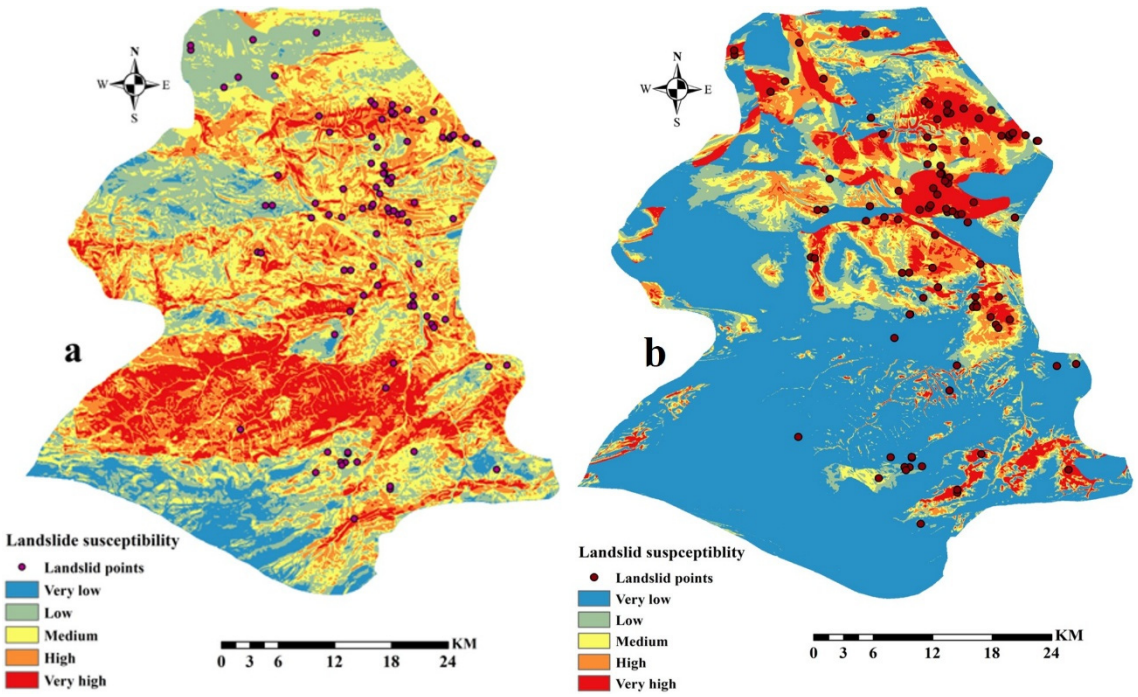


Figure 5. Landslide susceptibility areas map using BWM (**a**) and GraphSAGE-GAT (**b**).

3.3. Performance Analysis Between BWM and GraphSAGE-GAT

The distribution of landslide susceptibility classes obtained from BWM and GraphSAGE-GAT shows a substantial difference between the two approaches(Figure 6). The GraphSAGE-GAT model classified 62.03% of the study area as very low susceptibility, whereas this class accounted for only 6.44% in the BWM map. In contrast, BWM assigned a considerably larger proportion of the area to medium-, high-, and very-high-susceptibility classes (71.74% in total), compared with only 26.93% for GraphSAGE-GAT. Notably, the GraphSAGE-GAT results show a more concentrated spatial distribution of high-susceptibility areas, with 18.24% of the area classified as high or very high susceptibility. This difference indicates that GraphSAGE-GAT provides a more selective identification of potentially susceptible areas rather than broadly assigning moderate-to-high susceptibility across the study area.

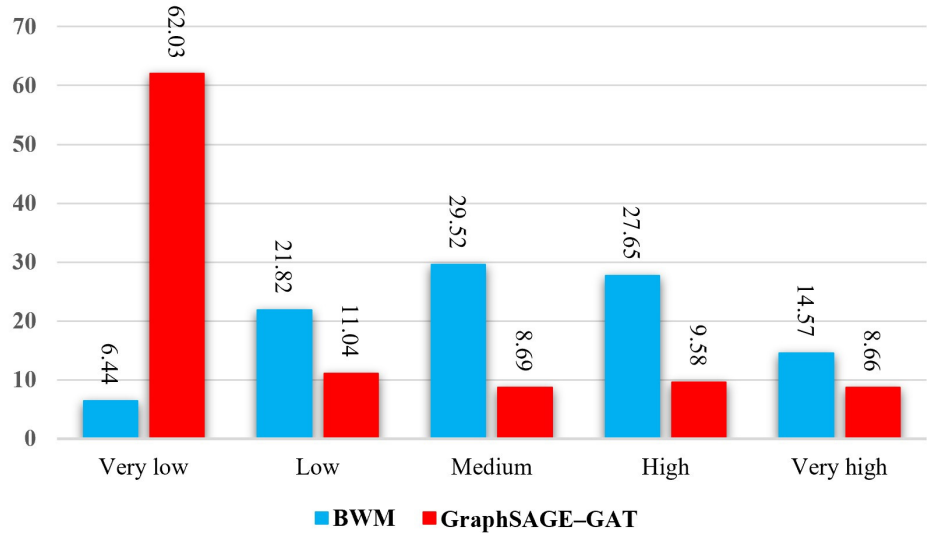


Figure 6. Percentage area of landslide susceptibility classes for the applied models.

Table 6 presents the distribution of the 101 observed landslide points among the five susceptibility classes generated by the BWM and GraphSAGE-GAT models. In the very-low- and low-susceptibility classes, BWM classified 24 landslide points, compared with 23 points identified by GraphSAGE-GAT. For the medium-susceptibility class, BWM included 30 landslide points, whereas GraphSAGE-GAT classified only 10 points in this category. A notable difference was observed in the high- and very-high-susceptibility classes, where 47 landslide points (46.53%) were identified by BWM, compared with 68 points (67.33%) by GraphSAGE-GAT. These results indicate that GraphSAGE-GAT was able to concentrate a substantially larger proportion of the observed landslide occurrences within the high- and very-high-susceptibility classes. This improved spatial correspondence suggests that the GraphSAGE-GAT model has a stronger capability to discriminate susceptible locations from less susceptible areas, which can be attributed to its ability to incorporate both environmental characteristics and spatial relationships among neighboring pixels.

Table 6. Number of landslide points in susceptibility classes.

Class / Algorithm	Very Low	Low	Medium	High	Very High
BWM	1	23	30	33	14
GraphSAGE-GAT	11	12	10	23	45

Figure 7 shows the Precision–Threshold curves for the BWM and GraphSAGE-GAT models. The Precision of BWM remains relatively stable at approximately 0.60 over a broad range of thresholds and gradually increases to a maximum value of about 73% at a threshold of approximately 0.60. Beyond this point, Precision decreases sharply, indicating a reduction in the reliability of positive predictions at higher thresholds. In contrast, GraphSAGE-GAT exhibits a gradual and generally increasing Precision pattern as the threshold increases, reaching approximately 100% at a threshold close to 1.0. This pattern indicates that increasing the decision threshold progressively reduces false-positive predictions in the GraphSAGE-GAT model, although the very high Precision at the extreme threshold should be interpreted cautiously because it may correspond to a small number of positive predictions. Overall, GraphSAGE-GAT demonstrates a more consistent improvement in Precision across the threshold range, whereas BWM reaches its optimum at an intermediate threshold and subsequently becomes less stable.

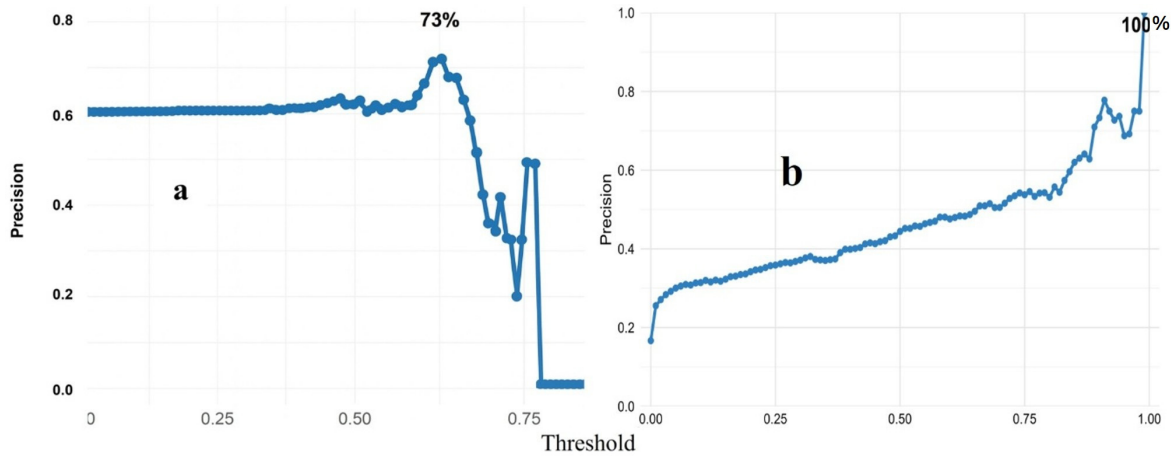


Figure 7. The Precision–Threshold plots for the two models: (**a**) BWM and (**b**) GraphSAGE-GAT.

Figure 8 illustrates the variations in Precision, Recall, and Specificity across different threshold values for the GraphSAGE-GAT and BWM models, highlighting the trade-off between correctly identifying landslide-prone areas and minimizing false-positive predictions. For the GraphSAGE-GAT model (Figure 8a), Recall is initially close to 1 at low threshold values, indicating that most observed landslide occurrences are successfully identified. As the threshold increases, Recall gradually decreases, while Specificity continuously increases, reflecting a progressive reduction in false-positive predictions. Precision also shows an increasing trend and reaches higher values at intermediate and high thresholds, although some fluctuations are observed at the upper end of the threshold range. This pattern indicates that GraphSAGE-GAT provides a flexible trade-off between Recall and Specificity depending on the selected susceptibility threshold. For the BWM model (Figure 8b), Recall remains close to 1 at low thresholds but begins to decline substantially as the threshold increases. In contrast, Specificity initially remains low and then increases progressively with increasing threshold values. Precision remains relatively stable at approximately 0.6 over a broad range of thresholds before increasing at higher threshold values, although it exhibits noticeable fluctuations near the upper threshold range. The convergence of Precision, Recall, and Specificity occurs within an intermediate threshold range, indicating a more balanced classification performance at these threshold values. Overall, comparison of the two models shows that GraphSAGE-GAT provides a more dynamic separation between susceptible and non-susceptible areas, while BWM exhibits a more gradual transition between Recall and Specificity. The results further demonstrate that threshold selection substantially affects the balance between detecting actual landslide occurrences and minimizing false alarms and therefore should be considered when applying the susceptibility maps for practical landslide sensitivity assessment.

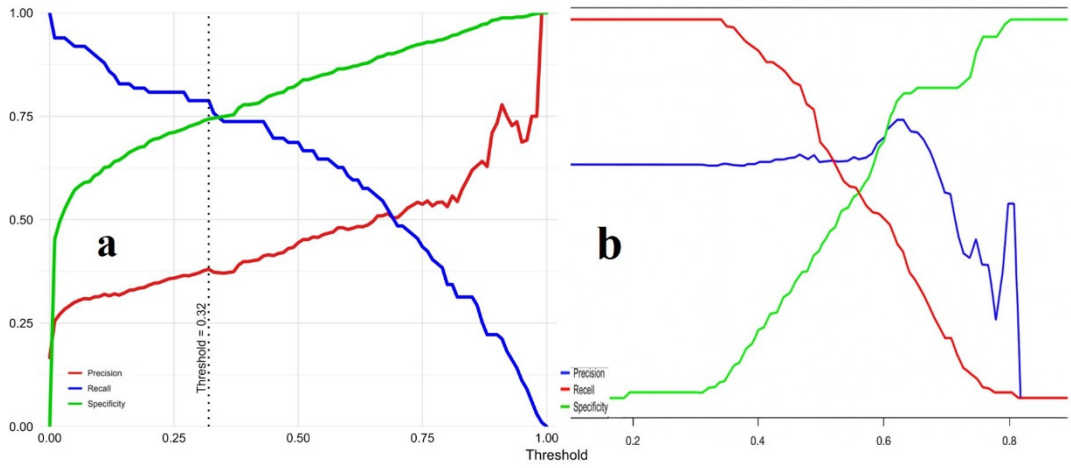


Figure 8. Changes in Precision (blue), Recall (red), and Specificity (green) with respect to the threshold: (**a**) GraphSAGE-GAT and (**b**) BWM.

Figure 9 compares the ROC curves and AUC values of the BWM and GraphSAGE-GAT models for landslide susceptibility prediction. The BWM model achieved an AUC of 0.544, which is only slightly higher than the random classification level (0.50), indicating a relatively weak ability to discriminate between susceptible and non-susceptible areas. In contrast, the GraphSAGE-GAT model achieved an AUC of 0.8360, demonstrating good discriminatory performance and a substantially higher ability to distinguish landslide-prone areas from stable areas. The considerable difference between the two AUC values highlights the advantage of incorporating spatial relationships and neighboring-node information through the GraphSAGE-GAT architecture. Overall, the ROC analysis indicates

that GraphSAGE-GAT provides considerably more reliable landslide susceptibility predictions than BWM.

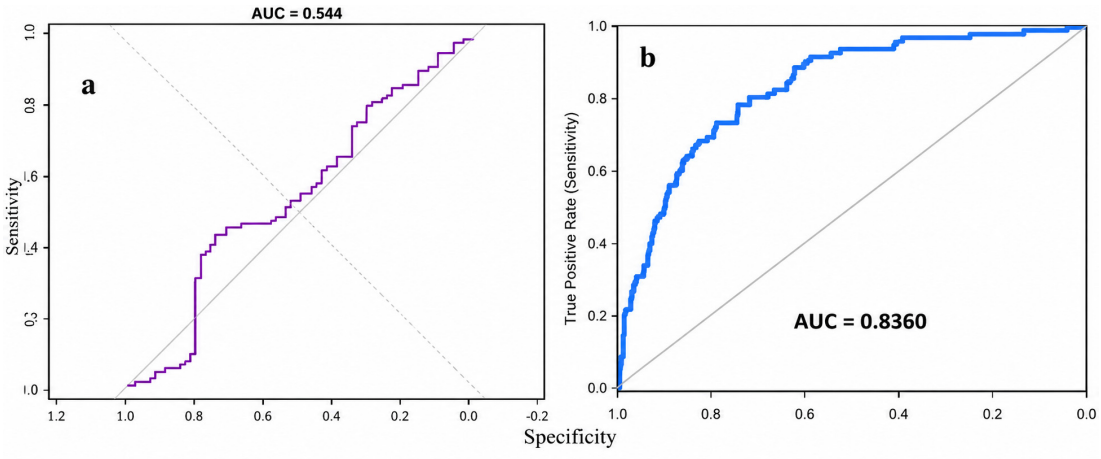


Figure 9. The AUC graph: (**a**) BWM and (**b**) GraphSAGE-GAT.

3.4. Discussion

Landslides can cause not only the destruction of human facilities but also the loss of many lives worldwide every year [75,76]. Savadkouh County suffers from considerable landslide susceptibility, and landslide risks have been evaluated in previous studies [77]. However, because both DL and MCDM approaches are widely used for landslide susceptibility assessment, their predictive performance needs to be evaluated within a consistent comparative framework [78,79]. Therefore, identifying a reliable approach for delineating landslide-susceptible areas is essential for effective hazard assessment and risk management. In this study, the BWM and GraphSAGE-GAT approaches were compared to evaluate their ability to predict landslide susceptibility. While BWM represents an expert-based MCDM approach, GraphSAGE-GAT integrates graph-based DL with an attention mechanism to capture both environmental characteristics and spatial relationships among neighboring pixels. Such a comparison provides a different perspective on the applicability of knowledge-driven and data-driven approaches for landslide susceptibility mapping [80,81].

The susceptibility maps generated by BWM and GraphSAGE-GAT show substantial differences in their spatial patterns across Savadkouh County. The BWM map indicates extensive areas of medium to very high susceptibility, particularly across the central and southern parts of the county, whereas GraphSAGE-GAT identifies a considerably larger proportion of the study area as very low susceptibility and concentrates high and very high susceptibility in more localized areas, particularly in the northern, northeastern, central, and eastern parts of the county. This difference is also reflected in the distribution of observed landslide points among the susceptibility classes. Of the 101 observed landslide points, BWM places 24 points (23.76%) within the very-low- and low-susceptibility classes, whereas GraphSAGE-GAT places 23 points (22.77%) within these classes. In contrast, 47 landslide points (46.53%) are located in the high- and very-high-susceptibility classes in the BWM map, compared with 68 points (67.33%) in the GraphSAGE-GAT map. Thus, GraphSAGE-GAT concentrates approximately 20.80 percentage points more of the observed landslide occurrences within the two highest susceptibility classes. Previous research in the study area reported that the VIKOR method placed approximately 73% of observed landslide events in high- and very-high-susceptibility areas [82], while the combination of AHP with a fuzzy gamma operator of 0.8 achieved an accuracy of approximately 70% [83]. These findings indicate that the spatial performance of landslide

susceptibility models can vary substantially depending on the underlying modeling framework. Kavzoglu et al. (2018) similarly demonstrated that machine learning approaches can provide higher predictive performance than traditional statistical methods in landslide susceptibility mapping [84]. More recently, hybrid intelligent frameworks combining multiple computational techniques have also been proposed for slope deformation and landslide-related prediction [85], highlighting the growing importance of data-driven and hybrid approaches for capturing the nonlinear and spatially complex behavior of landslides.

The comparison of the two models demonstrates notable differences in both susceptibility-class distribution and the spatial allocation of observed landslide occurrences. Although BWM assigns only 6.44% and 21.82% of the study area to the very-low- and low-susceptibility classes, respectively, 24 observed landslide points still occur within these two classes. More importantly, only 46.53% of the observed landslide points are located within the high- and very-high-susceptibility classes. In contrast, GraphSAGE-GAT assigns 62.03% of the study area to the very-low-susceptibility class and identifies more localized high-susceptibility zones. Despite the substantially smaller proportion of the study area classified as high and very high susceptibility, 67.33% of the observed landslide points are concentrated within these two classes. This finding suggests that GraphSAGE-GAT is more selective in delineating susceptible areas and is less likely to classify extensive portions of the study area as moderate-to-high susceptibility. The stronger concentration of observed landslides within the highest susceptibility classes is particularly important for practical landslide screening because it allows potentially hazardous locations to be prioritized more effectively.

The threshold-based evaluation further supports the differences between the two approaches. For BWM, Precision remains approximately 0.60 over a broad range of threshold values and reaches a maximum of about 0.73 at a threshold of approximately 0.60 before declining sharply. GraphSAGE-GAT, in contrast, shows a generally increasing Precision trend with increasing threshold values and approaches 100% Precision at thresholds close to 1.0. However, this extreme Precision value should be interpreted cautiously because very high thresholds correspond to a smaller number of positive predictions. The Precision–Recall–Specificity analysis further demonstrates the trade-off between identifying observed landslides and reducing false-positive predictions. GraphSAGE-GAT shows high Recall at low thresholds, while Specificity progressively increases as the threshold becomes more restrictive. This behavior indicates that the model provides flexibility in selecting a threshold according to the relative importance of landslide detection versus false-alarm reduction. BWM also exhibits a trade-off between Recall and Specificity, but its performance becomes less stable at higher threshold values. The threshold analysis suggests that GraphSAGE-GAT provides a more effective basis for differentiating between susceptible and non-susceptible areas, although the final operational threshold should be selected according to the intended management objective.

The ROC analysis provides further evidence of the difference in discriminatory performance between the two approaches. The BWM model achieved an AUC of 0.544, which is only slightly above the random classification level of 0.50 and indicates limited discrimination between landslide-prone and non-landslide-prone locations. In contrast, GraphSAGE-GAT achieved an AUC of 0.8360, demonstrating good discriminatory capability. The substantial difference between the two AUC values indicates that GraphSAGE-GAT can distinguish susceptible and non-susceptible locations considerably more effectively than BWM. This result is also consistent with the distribution of observed landslide points, where a greater proportion of events is concentrated in the high- and very-high-susceptibility classes in the GraphSAGE-GAT output. Therefore, the ROC analysis, susceptibility-class distribution, and spatial correspondence with observed landslides

collectively indicate that GraphSAGE-GAT provides a more effective predictive framework than BWM for the study area.

The comparatively lower performance of BWM can be attributed to the characteristics of the method itself. BWM relies on expert judgment to determine the relative importance of conditioning factors, and the resulting weights remain fixed across the study area. Although this approach provides a transparent and interpretable framework for integrating multiple environmental factors, fixed global weights may not fully represent the complex and spatially heterogeneous interactions governing landslide occurrence. The conditioning factors considered in this study are diverse in nature and may interact nonlinearly, meaning that their combined influence may vary spatially. Consequently, a weight-based MCDM framework may have difficulty representing localized combinations of terrain, environmental, and anthropogenic conditions associated with landslide occurrence.

In contrast, the superior performance of GraphSAGE-GAT can be attributed to its ability to learn both feature-level relationships and spatial dependencies directly from the data. In the proposed architecture, GraphSAGE aggregates information from the nearest neighboring pixels, allowing the representation of each pixel to incorporate its local spatial context rather than relying solely on its individual environmental characteristics. The subsequent GAT layer further improves this process by assigning adaptive attention weights to neighboring nodes, allowing more informative spatial relationships to contribute more strongly to the final representation. This mechanism is particularly relevant to landslide susceptibility because landslide occurrence is spatially dependent and is often controlled by combinations of neighboring terrain and environmental conditions rather than by isolated pixel characteristics. The improved AUC of 0.8360 and the concentration of 67.33% of observed landslides in the high- and very-high-susceptibility classes provide quantitative evidence that incorporating these spatial relationships can substantially improve susceptibility discrimination. Overall, the results demonstrate that while BWM offers a transparent expert-based framework for susceptibility assessment, GraphSAGE-GAT provides a more adaptive and spatially responsive approach for identifying landslide-prone areas in Savadkouh County.

Limitations and Uncertainties

Several limitations and uncertainties should be acknowledged in this study. First, the landslide inventory comprised 101 recorded events provided by the Geological Survey of Iran. Limited access to the original survey records and detailed inventory metadata restricted independent verification of the temporal characteristics and positional accuracy of individual landslides. Second, the random selection of non-landslide samples, the maximum 20:1 negative-to-positive sampling ratio, and the absence of spatial constraints may have introduced sampling bias and spatial dependence into model evaluation. Third, the GraphSAGE–GAT model depends on methodological choices, including feature-space K-nearest-neighbor graph construction (K = 10), network architecture, and training parameters. The sensitivity of the results to alternative graph configurations and hyperparameters was not systematically assessed. Finally, although the selected conditioning factors represent important environmental and anthropogenic controls on landslides, uncertainties in the source data, spatial resolution, thematic classification, and potential correlations among factors may affect the resulting susceptibility maps. Future research should incorporate more comprehensive inventories, spatially independent validation, sensitivity analysis, and systematic assessment of factor dependence to improve the reliability and generalizability of landslide susceptibility predictions.

4. Conclusions

LSM has been widely used as an important basis for risk assessment, land-use planning, and hazard management to reduce the potential socio-environmental impacts of landslides. This study integrated GIS with BWM and GraphSAGE-GAT to generate and compare LSMs for Savadkouh County, northern Iran. BWM represents a knowledge-driven approach based on expert judgment, whereas GraphSAGE-GAT uses supervised deep learning to identify relationships among neighboring nodes and their conditioning factors. The results showed that 68 of the 101 observed landslide points (67.33%) fell within the high- and very-high-susceptibility classes in the GraphSAGE-GAT map, compared with 47 points (46.53%) in the BWM map. GraphSAGE-GAT achieved an area under the ROC curve (AUC) of 0.8360, substantially higher than the BWM value of 0.544. The threshold-based analysis also showed that GraphSAGE-GAT Precision approached 100% at very high thresholds, while BWM reached a maximum of approximately 73%. However, these Precision values should be interpreted alongside other evaluation metrics, particularly at extreme thresholds. The stronger discriminatory performance of GraphSAGE-GAT may be associated with its ability to aggregate neighborhood information through GraphSAGE and assign different importance to neighboring nodes through the GAT attention mechanism. Although these results suggest better discrimination by GraphSAGE-GAT under the evaluation procedure used, they should be interpreted cautiously because the random train–test split does not ensure spatial independence between the training and test samples. The use of feature-space neighborhoods may enable GraphSAGE-GAT to learn relationships among environmental conditioning factors; however, the contribution of this mechanism to predictive performance requires further assessment using independent spatial validation. Specifically, future studies could provide experts with a subset of positive (landslide) and negative (non-landslide) samples to inform their assessment and comparison of the conditioning factors, thereby exploring ways to incorporate empirical evidence into expert-based evaluations. Furthermore, integrating expert knowledge from BWM with graph-based deep learning models could provide a promising hybrid framework that combines the interpretability of expert-based decision-making with the spatial learning capability of GNNs. Such approaches could subsequently be evaluated in other landslide-prone regions to assess their generalizability and robustness.

Author Contributions: Conceptualization, A.H., S.S.F., M.K., M.M. and J.W.; Methodology, A.H., M.K., P.S. M.M. and J.W.; Software, A.H. S.S.F., M.M. and P.S.; Validation, A.H., M.K. and M.M.; Formal Analysis, A.H., and S.S.F.; Investigation, S.S.F., M.K., P.S., M.M. and A.D.; Data Curation, A.H., S.S.F., M.M. and A.D.; Writing—Original Draft, A.H., P.S., M.M. and J.W.; Writing—Review and Editing, A.H., S.S.F., M.K., P.S., M.M., A.D. and J.W.; Visualization, A.H. S.S.F. and M.M.; Supervision, J.W.; Project Administration, M.M. All authors have read and agreed to the published version of the manuscript.

Funding: This research received no external funding.

Data Availability Statement: The data are available upon request.

Conflicts of Interest: The authors declare no conflicts of interest.

References

1. Zhao, K.; Qiu, H.; Liu, Y.; Liu, Z.; Zhu, Y.; Yang, G.; Luo, W.; Li, Z. Rainfall threshold-governed landslide susceptibility in the Himalaya. *J. Hydrol. Reg. Stud.* **2026**, *68*, 104097.
2. Turner, A.K. Social and environmental impacts of landslides. *Innov. Infrastruct. Solut.* **2018**, *3*, 70.
3. Fidan, S.; Tanyaş, H.; Akbaş, A.; Lombardo, L.; Petley, D.N.; Görüm, T. Understanding fatal landslides at global scales: A summary of topographic, climatic, and anthropogenic perspectives. *Nat. Hazards* **2024**, *120*, 6437–6455.

4. Steger, S.; Moreno, M.; Crespi, A.; Zellner, P.J.; Gariano, S.L.; Brunetti, M.T.; Melillo, M.; Peruccacci, S.; Marra, F.; Kohrs, R.; et al. Deciphering seasonal effects of triggering and preparatory precipitation for improved shallow landslide prediction using generalized additive mixed models. *Nat. Hazards Earth Syst. Sci. Discuss.* **2022**, *12*, 1483–1506.
5. Gariano, S.L.; Guzzetti, F. Landslides in a changing climate. *Earth-Sci. Rev.* **2016**, *162*, 227–252.
6. Zhang, J.; Ma, X.; Zhang, J.; Sun, D.; Zhou, X.; Mi, C.; Wen, H. Insights into geospatial heterogeneity of landslide susceptibility based on the SHAP-XGBoost model. *J. Environ. Manag.* **2023**, *332*, 117357.
7. Dhakal, D.; Singh, K.; Onyelowe, K.C.; Cazco, S.A.S.; Sharma, A.; Alarifi, N.; Islam, F.; Arunachalam, K.P.; Youssef, Y.M. Enhancing landslide disaster prediction by evaluating non-landslide area sampling in machine learning models for Spiti Valley, India. *Sci. Rep.* **2025**, *15*, 12242.
8. Zhou, D.; Zhao, Z.; Xi, W.; Zhao, X.; Chao, J. New method for landslide susceptibility evaluation in alpine valley regions that considers the suitability of InSAR monitoring and introduces deformation rate grading. *Geo-Spat. Inf. Sci.* **2025**, *28*, 565–588.
9. Alimohammadlou, Y.; Najafi, A.; Yalcin, A. Landslide process and impacts: A proposed classification method. *Catena* **2013**, *104*, 219–232.
10. Maleki, M.; Rahmati, M.; Sadidi, J.; Babaee, E. Landslide risk zonation using AHP method and GIS in Malaverd catchment, Kermanshah, Iran. In Proceedings of the International Conference on Geospatial Information Research (GI Research 2014), Tehran, Iran, 15–17 November 2014; pp. 15–17.
11. Ehteshami-Moinabadi, M. Properties of fault zones and their influences on rainfall-induced landslides, examples from Alborz and Zagros ranges. *Environ. Earth Sci.* **2022**, *81*, 168.
12. Ehsan, M.; Anees, M.T.; Bakar, A.F.B.A.; Ahmed, A. A review of geological and triggering factors influencing landslide susceptibility: Artificial intelligence-based trends in mapping and prediction. *Int. J. Environ. Sci. Technol.* **2025**, *22*, 17347–17382.
13. Casagli, N.; Intrieri, E.; Tofani, V.; Gigli, G.; Raspini, F. Landslide detection, monitoring and prediction with remote-sensing techniques. *Nat. Rev. Earth Environ.* **2023**, *4*, 51–64.
14. Lacasse, S.; Nadim, F. Landslide risk assessment and mitigation strategy. In *Landslides—Disaster Risk Reduction*; Springer: Berlin/Heidelberg, Germany, 2009; pp. 31–61.
15. Korup, O.; Stolle, A. Landslide prediction from machine learning. *Geol. Today* **2014**, *30*, 26–33.
16. Pollock, W.; Wartman, J. Human vulnerability to landslides. *GeoHealth* **2020**, *4*, e2020GH000287.
17. Marín-Rodríguez, N.J.; Vega, J.; Zanabria, O.B.; González-Ruiz, J.D.; Botero, S. Towards an understanding of landslide risk assessment and its economic losses: A scientometric analysis. *Landslides* **2024**, *21*, 1865–1881.
18. Metternicht, G.; Hurni, L.; Gogu, R. Remote sensing of landslides: An analysis of the potential contribution to geo-spatial systems for hazard assessment in mountainous environments. *Remote Sens. Environ.* **2005**, *98*, 284–303.
19. Sarkar, S.; Kanungo, D.P.; Patra, A.K.; Kumar, P. GIS based spatial data analysis for landslide susceptibility mapping. *J. Mt. Sci.* **2008**, *5*, 52–62.
20. Liu, S.; Wang, L.; Zhang, W.; He, Y.; Pijush, S. A comprehensive review of machine learning-based methods in landslide susceptibility mapping. *Geol. J.* **2023**, *58*, 2283–2301.
21. Ado, M.; Amitab, K.; Maji, A.K.; Jasińska, E.; Gono, R.; Leonowicz, Z.; Jasiński, M. Landslide susceptibility mapping using machine learning: A literature survey. *Remote Sens.* **2022**, *14*, 3029.
22. Wang, X.; Xie, H. A review on applications of remote sensing and geographic information systems (GIS) in water resources and flood risk management. *Water* **2018**, *10*, 608.
23. Tomaszewski, B. *Geographic Information Systems (GIS) for Disaster Management*; Routledge: London, UK, 2020.
24. Arvin, M.; Sohrabi, P.; Kianfar, N.; Amanpour, S.; Abdeyazdan, H.; Shirali, M.; Zandsalimi, M.; Esmailzadeh, A. The interlinkages between urban structure and COVID-19: A case study of Ahvaz. *Preprint* **2025**, https://doi.org/10.20944/preprints202503.1089.v1.
25. Farzad, R.; Brewick, P. A systematic sensitivity analysis workflow for hysteretic systems: Applications to biaxial Bouc–Wen models. *Nonlinear Dyn.* **2026**, *114*, 670.
26. Mobasheri, P.; Aranizadeh, A.; Vahidi, B. A hybrid signal-dynamics health index fusion framework for prognostics of small-scale wind turbine blades. *Sci. Rep.* **2026**, *16*, 31509.
27. Salehpour Jam, A.; Mosaffaie, J.; Sarfaraz, F.; Shadfar, S.; Akhtari, R. GIS-based landslide susceptibility mapping using hybrid MCDM models. *Nat. Hazards.* **2021**, *108*, 1025–1046.
28. Azarafza, M.; Azarafza, M.; Akgün, H.; Atkinson, P.M.; Derakhshani, R. Deep learning-based landslide susceptibility mapping. *Sci. Rep.* **2021**, *11*, 24112.

29. Kolios, A.; Mytilinou, V.; Lozano-Minguez, E.; Salonitis, K. A comparative study of multiple-criteria decision-making methods under stochastic inputs. *Energies* **2016**, *9*, 566.
30. Nyimbili, P.H.; Erden, T.; Karaman, H. Integration of GIS, AHP and TOPSIS for earthquake hazard analysis. *Nat. Hazards* **2018**, *92*, 1523–1546.
31. Hosseini, J.; Shakeryari, M.; Nazari Nejad, A.; Mastalizadeh, H.; Maleki, M.; Wang, J.; Rustum, R.; Rahmati, M.; Doostvandi, F.; Mostafavi, M.A. Comparison of the analytic network process and the best–worst method in ranking urban resilience and regeneration prioritization by applying geographic information systems. *Land* **2024**, *13*, 1008.
32. Singh, S.S.; Jeganathan, C. Examining the role of geospatial technologies and AI in disaster risk management and response, including hazard mapping, vulnerability assessment, and real-time monitoring. In *Advanced Geospatial Intelligence and AI for Environmental Resilience and Sustainable Development*; Springer Nature Switzerland: Cham, Switzerland, 2026; pp. 335–366.
33. Shirmohammadi, M.; Pirasteh, S.; Li, H.; Akhavan, M.; Isazadeh, V.; Ji, J.; Chen, C.; Muhammad, Y. Challenges and opportunities in flood mapping and modeling of next-generation geospatial intelligence: A review. *Geomat. Nat. Hazards Risk* **2026**, *17*, 2660866.
34. Mienye, I.D.; Swart, T.G. A comprehensive review of deep learning: Architectures, recent advances, and applications. *Information* **2024**, *15*, 755.
35. Sameen, M.I.; Pradhan, B.; Lee, S. Application of convolutional neural networks featuring Bayesian optimization for landslide susceptibility assessment. *Catena* **2020**, *186*, 104249.
36. Wang, Y.; Fang, Z.; Wang, M.; Peng, L.; Hong, H. Comparative study of landslide susceptibility mapping with different recurrent neural networks. *Comput. Geosci.* **2020**, *138*, 104445.
37. Zhang, Q.; He, Y.; Zhang, L.; Lu, J.; Gao, B.; Yang, W.; Chen, H.; Zhang, Y. A landslide susceptibility assessment method considering the similarity of geographic environments based on graph neural network. *Gondwana Res.* **2024**, *132*, 323–342.
38. Wu, Z.; Pan, S.; Chen, F.; Long, G.; Zhang, C.; Yu, P.S. A comprehensive survey on graph neural networks. *IEEE Trans. Neural Netw. Learn. Syst.* **2021**, *32*, 4–24.
39. Golkarieh, A.; Sassani, M.; Khamoushi, S.; Entezami, M.; Basirat, S. Intracranial hemorrhage diagnosis using deep learning: A survey of techniques, frameworks, and challenges. *Comput. Decis. Mak. Int. J.* **2026**, *3*, 780–804.
40. Gigović, L.; Drobnjak, S.; Pamučar, D. The application of the hybrid GIS spatial multi-criteria decision analysis best–worst methodology for landslide susceptibility mapping. *ISPRS Int. J. Geo-Inf.* **2019**, *8*, 79.
41. Moharrami, M.; Naboureh, A.; Gudiyangada Nachappa, T.; Ghorbanzadeh, O.; Guan, X.; Blaschke, T. National-scale landslide susceptibility mapping in Austria using fuzzy best-worst multi-criteria decision-making. *ISPRS Int. J. Geo-Inf.* **2020**, *9*, 393.
42. Ghorbanzadeh, O.; Blaschke, T.; Gholamnia, K.; Meena, S.R.; Tiede, D.; Aryal, J. Evaluation of different machine learning methods and deep-learning convolutional neural networks for landslide detection. *Remote Sens.* **2019**, *11*, 196.
43. Prakash, N.; Manconi, A.; Loew, S. Mapping landslides on EO data: Performance of deep learning models vs. traditional machine learning models. *Remote Sens.* **2020**, *12*, 346.
44. Gholami Brenjstanaki, M.; Sharifiniya, Z. Ranking the investment in the sample tourism districts: Case study of Savadkuh Township. *Geogr. (Reg. Plan.)* **2018**, *8*, 55–72.
45. Ghasemi, J.; Gholami, H.; Afzaligrouh, A.; Alambeigi, A. Analyzing ecotourism effects on local communities' empowerment (case study: Savadkuh County). *J. Environ. Educ. Sustain. Dev.* **2023**, *11*, 87–106.
46. Karami, A.; Mohamadi, Z.; Rastegari, H.; Savadkouhi, A.S. Evaluation of the sustainability of rural areas and application of the Delphi fuzzy technique and the artificial neural network: A case study of rural areas of northern Savadkouh County. *J. Rural Res.* **2018**, *9*, 496–511.
47. Zou, Q.; Jiang, H.; Cui, P.; Zhou, B.; Jiang, Y.; Qin, M.; Liu, Y.; Li, C. A new approach to assess landslide susceptibility based on slope failure mechanisms. *Catena* **2021**, *204*, 105388.
48. Segoni, S.; Pappafico, G.; Luti, T.; Catani, F. Landslide susceptibility assessment in complex geological settings: Sensitivity to geological information and insights on its parameterization. *Landslides* **2020**, *17*, 2443–2453.
49. Demir, G.; Aytekin, M.; Akgün, A.; Ikizler, S.B.; Tatar, O. A comparison of landslide susceptibility mapping of the eastern part of the North Anatolian Fault Zone (Turkey) by likelihood-frequency ratio and analytic hierarchy process methods. *Nat. Hazards* **2013**, *65*, 1481–1506.
50. Huang, F.; Chen, J.; Liu, W.; Huang, J.; Hong, H.; Chen, W. Regional rainfall-induced landslide hazard warning based on landslide susceptibility mapping and a critical rainfall threshold. *Geomorphology* **2022**, *408*, 108236.
51. Li, Y.; Duan, W. Decoding vegetation's role in landslide susceptibility mapping: An integrated review of techniques and future directions. *Biogeotechnics* **2024**, *2*, 100056.

52. Huang, F.; Xiong, H.; Yao, C.; Catani, F.; Zhou, C.; Huang, J. Uncertainties of landslide susceptibility prediction considering different landslide types. *J. Rock Mech. Geotech. Eng.* **2023**, *15*, 2954–2972.
53. Pourghasemi, H.R.; Pradhan, B.; Gokceoglu, C.; Deylami Moezzi, K. Landslide susceptibility mapping using a spatial multi-criteria evaluation model at Haraz Watershed, Iran. In *Terrigenous Mass Movements: Detection, Modelling, Early Warning and Mitigation Using Geoinformation Technology*; Springer: Berlin/Heidelberg, Germany, 2012; pp. 23–49.
54. Chen, W.; Li, Y. GIS-based evaluation of landslide susceptibility using hybrid computational intelligence models. *Catena* **2020**, *195*, 104777.
55. Puente-Sotomayor, F.; Mustafa, A.; Teller, J. Landslide susceptibility mapping of urban areas: Logistic regression and sensitivity analysis applied to Quito, Ecuador. *Geoenviron. Disasters* **2021**, *8*, 19.
56. Wang, Y.; Wu, X.; Lin, G.; Peng, B. Deciphering the social vulnerability of landslides using the coefficient of variation-Kullback-Leibler-TOPSIS at an administrative village scale. *Remote Sens.* **2025**, *17*, 714.
57. Zhang, T.; Wang, D.; Lu, Y. Machine learning-enabled regional multi-hazards risk assessment considering social vulnerability. *Sci. Rep.* **2023**, *13*, 13405.
58. Shibasaki, T.; Matsuura, S.; Hasegawa, Y. Temperature-dependent residual shear strength characteristics of smectite-bearing landslide soils. *J. Geophys. Res. Solid Earth* **2017**, *122*, 1449–1469.
59. Rezaei, J. Best-worst multi-criteria decision-making method. *Omega* **2015**, *53*, 49–57.
60. Sohrabi, P.; Taheri, J.; Nasiri, B.; Borna, M.; Soltannia, R. Assessment of the quality of life in Tehran: A comparison of multi-criteria decision-making methods using GIS. *Sci. Conserv. Archaeol.* **2026**, *38*, 259–274.
61. Maleki, M.; Salman, M.; Sahebi Vayghan, S.; Szabo, S. GIS-based sinkhole susceptibility mapping using the best worst method. *Spat. Inf. Res.* **2023**, *31*, 537–545.
62. Jorshary, K.M.; Sassani, M.; Raoufi, S.; Khamoushi, S. Ranking of AI-driven strategies for optimizing the health tourism supply chain using stratified BWM. *Knowl. Decis. Syst. Appl.* **2025**, *1*, 295–315.
63. Wu, L. Towards trustworthy graph neural networks and their applications in recommender systems. In *Proceedings of the 2024 IEEE International Conference on Big Data (BigData)*; IEEE: New, NY, USA, 2024; pp. 8250–8252.
64. Wu, X.; Ren, X.; Zhai, D.; Wang, X.; Tarif, M. Lights-transformer: An efficient transformer-based landslide detection model for high-resolution remote sensing images. *Sensors* **2025**, *25*, 3646.
65. Hamilton, W.; Ying, Z.; Leskovec, J. Inductive representation learning on large graphs. In *Advances in Neural Information Processing Systems*; MIT Press: Cambridge, MA, USA, 2017; Volume 30.
66. Veličković, P.; Cucurull, G.; Casanova, A.; Romero, A.; Lio, P.; Bengio, Y. Graph attention networks. *arXiv* **2017**, arXiv:1710.10903.
67. Nahm, F.S. Receiver operating characteristic curve: Overview and practical use for clinicians. *Korean J. Anesthesiol.* **2022**, *75*, 25–36.
68. Hwang, Y.T.; Hsu, Y.R.; Su, N.C. Performance of tests based on the area under the ROC curve for multireader diagnostic data. *J. Appl. Stat.* **2025**, *52*, 555–577.
69. Carroll, H.D.; Kann, M.G.; Sheetlin, S.L.; Spouge, J.L. Threshold Average Precision (TAP-k): A measure of retrieval designed for bioinformatics. *Bioinformatics* **2010**, *26*, 1708–1713.
70. Berger, A.; Guda, S. Threshold optimization for F measure of macro-averaged precision and recall. *Pattern Recognit.* **2020**, *102*, 107250.
71. Bhat, S.; Mansoor, A.; Georgescu, B.; Panambur, A.B.; Ghesu, F.C.; Islam, S.; Packhäuser, K.; Rodríguez-Salas, D.; Grbic, S.; Maier, A. AUCReshaping: Improved sensitivity at high-specificity. *Sci. Rep.* **2023**, *13*, 21097.
72. De Figueiredo, M.; Cordella, C.B.; Bouveresse, D.J.R.; Archer, X.; Bégué, J.M.; Rutledge, D.N. A variable selection method for multiclass classification problems using two-class ROC analysis. *Chemom. Intell. Lab. Syst.* **2018**, *177*, 35–46.
73. Han, H. The utility of receiver operating characteristic curve in educational assessment: Performance prediction. *Mathematics* **2022**, *10*, 1493.
74. Camacho, M.; Romeu, A.; Ramallo, S. Probabilistic classification in business cycles identification based on generalized ROC. *J. Forecast.* **2025**, *45*, 3–21.
75. Wang, Y.; Nanehkaran, Y.A. GIS-based fuzzy logic technique for mapping landslide susceptibility analyzing in a coastal soft rock zone. *Nat. Hazards* **2024**, *120*, 10889–10921.
76. Amarasinghe, M.P.; Kulathilaka, S.A.S.; Robert, D.J.; Zhou, A.; Jayathissa, H.A.G. Risk assessment and management of rainfall-induced landslides in tropical regions: A review. *Nat. Hazards* **2024**, *120*, 2179–2231.

77. Abdollahi, M.S.; Soltaninejad, S.; Naveen, B.P. Comprehensive numerical analysis of landslide risk management: A case study of the Jiroft Dam. *Innov. Infrastruct. Solut.* **2026**, *11*, 214.
78. Ngo, P.T.T.; Panahi, M.; Khosravi, K.; Ghorbanzadeh, O.; Kariminejad, N.; Cerda, A.; Lee, S. Evaluation of deep learning algorithms for national scale landslide susceptibility mapping of Iran. *Geosci. Front.* **2021**, *12*, 505–519.
79. Farzad, R.; Brewick, P. Interpretable β-variational autoencoders for discovering higher-order sensitivities in nonlinear hysteretic structures. *J. Eng. Mech.* **2026**, *152*, 04026067.
80. Maleki, M.; Tavakkoli Sabour, S.M.; Zeaieanfirouzabadi, P.; Raeisi, M. Comparison of optic and radar data for terrain feature extraction. *J. RS GIS Nat. Resour.* **2018**, *9*, 93–107.
81. Wan, S.; Li, T.; Ma, J.; Meng, L.; Wang, H.; Yuan, F. Bridging data-driven intelligence and expert-driven knowledge: A systematic review of the RF-AHP hybrid paradigm. *WIREs Data Min. Knowl. Discov.* **2026**, *16*, e70107.
82. Dehnavi Eelagh, M.; Pahlavani, P. Landslide susceptibility assessment using VIKOR and ordered weighted averaging methods: A case study of Savadkuh County. *Phys. Geogr. Res.* **2024**, *56*, 41–59.
83. Arekhi, S.; Akbarian Sorkhi, M.; Emadaddian, S. Landslide risk modeling using fuzzy hierarchical analysis: The case study of Savadkuh city. *Geogr. Plan. Space* **2024**, *14*, 171–195.
84. Kavzoglu, T.; Colkesen, I.; Sahin, E.K. Machine learning techniques in landslide susceptibility mapping: A survey and a case study. In *Landslides: Theory, Practice and Modelling*; Springer: Cham, Switzerland, 2018; pp. 283–301.
85. Meng, J.; Li, J.P.; Jiang, S.H.; Huang, J.; Wang, Y. Random particle finite element method for probabilistic slope large-deformation analysis accounting for spatial variability. *J. Rock Mech. Geotech. Eng.* 2025, *in press*.

Disclaimer/Publisher's Note: The statements, opinions and data contained in all publications are solely those of the individual author(s) and contributor(s) and not of MDPI and/or the editor(s). MDPI and/or the editor(s) disclaim responsibility for any injury to people or property resulting from any ideas, methods, instructions or products referred to in the content.